Large range dual-axis micro-stage driven by electrostatic comb-drive actuators

2013 J. Micromech. Microeng. 23 105008

(http://iopscience.iop.org/0960-1317/23/10/105008)

J. Micromech. Microeng. **23** (2013) 105008 (11pp) doi:10.1088/0960-1317/23/10/105008

Large range dual-axis micro-stage driven by electrostatic comb-drive actuators

Mohammad Olfatnia, Leqing Cui, Pankaj Chopra and Shorya Awtar

Precision Systems Design Laboratory, Mechanical Engineering, University of Michigan, Ann Arbor, MI 48109, USA

E-mail: awtar@umich.edu

Received 19 April 2013, in final form 22 July 2013
Published 10 September 2013
Online at stacks.iop.org/JMM/23/105008

Abstract

This paper presents a micro *XY* stage that employs electrostatic comb-drive actuators and achieves a bi-directional displacement range greater than 225 μm per motion axis. The proposed *XY* stage design comprises four rigid stages (ground, motion stage, and two intermediate stages) interconnected via flexure modules. The motion stage, which has two translational degrees of freedom, is connected to two independent single degree of freedom intermediate stages via respective parallelogram (P) transmission flexures. The intermediate stages are connected to the ground via respective clamped paired double parallelogram (C-DP-DP) guidance flexures. The C-DP-DP flexure, unlike conventional flexures such as the paired double parallelogram flexure (DP-DP), provides high bearing direction stiffness (K_b) while maintaining low motion direction stiffness (K_m) over a large range of motion direction displacement. This helps delay the onset of sideways instability in the comb-drive actuators that are integrated with the intermediate stages, thereby offering a significantly greater actuation stroke compared to existing designs. The presented work includes closed-form stiffness analysis of the proposed micro-stage, finite elements simulation, and experimental measurements of its static and dynamic behavior.

(Some figures may appear in colour only in the online journal)

1. Introduction and background

Micro *XY* motion stages that allow large ranges of motion ($\geqslant$100 μm) are desirable in several applications such as probe-based data-storage systems [1–3], scanning probe microscopy [4], and optical sensing and communication systems [5]. One limitation of the existing micro *XY* stages is their relatively small range of motion. Although large range single-axis flexure stages have been reported [6–8], a similar range has not been seen in micro *XY* stages so far.

Various actuation schemes such as piezoelectric, electromagnetic, electrothermal and electrostatic [9], have been implemented in microelectromechanical systems (MEMS)/micro-stages. Table 1 compares the stroke, footprint, resonant frequency and amplification ratio for some representative micro-actuators reported in the literature. Electromagnetic actuation is common because of its linear electrical input versus displacement output curve and its relatively low actuation voltage. However, design and fabrication of a MEMS electromagnetic actuator with sufficient magnetic material mass and coil turns that are capable of generating desired force and displacement is difficult. Hybrid integration, i.e. assembling conventional electromagnetic actuators with a micro-fabricated MEMS device, has been generally used to overcome this problem; for instance, see the IBM millipede data-storage system with a stroke of 120 μm [1].

Electrothermal actuators are easily fabricated from a single material, and generally employ either two connected arms with different cross sections (cold–hot arm thermal actuator [10]) to obtain differential thermal expansion or a stack of expansion arms placed symmetrically on either side of a movable central shuttle (v-shaped chevron thermal actuator [11]). The thermal expansion in these actuators provides a strong actuation force but a small deflection of the order of a few micrometers, for instance 5 μm in [11]. One may achieve large displacement in thermal actuators by employing large beam lengths. For instance, Syms [12] reported a displacement of 500 μm at the resonant condition using an electrothermal actuator with a suspended beam length of 15 mm. This large

Table 1. Comparison of some representative single-axis micro-actuators.

Reference	Actuator type	Stroke (μm)	Footprint (mm^2)	Resonant frequency (Hz)	Amplification ratio
[17]	Piezoelectric	1	1	20×10^3	3.33 ×
[14]	Piezoelectric	486	1.8	507	170 ×
[18]	Electromagnetic	120	3.4	175	N/A
[19]	Electrostatic	20	0.02	3.8×10^3	12 ×
[6]	Electrostatic	180	4	769	N/A
[12]	Electrothermal	500	18	100	16 ×
[20]	Electrothermal	100	4	Not reported	21 ×

footprint, along with its large thermal time constant, degrades the dynamic performance of these actuators; for instance, resonant frequency of the Syms actuator was around 100 Hz. Moreover, the power dissipation and high working temperature (200°–600° C) are other two undesirable properties of thermal actuators [13].

Piezoelectric actuators consume considerably less power and provide large mechanical forces and high resonant frequencies in a compact design; however, the primary limitation of these actuators is their inherently small stroke, typically of the order of a few micrometers [14]. A relative expansion (or strain) of up to 0.2% is achievable with piezo stack actuators [15]. In an attempt to overcome the limited motion range in the above-mentioned actuation schemes, actuators may be integrated with displacement amplifier mechanisms [16]. However, amplifying the motion range reduces the output force and bandwidth of the system. Moreover, the use of amplification mechanisms often leads to large device foot-prints [14].

Electrostatic comb-drive microactuators are well established in the MEMS field because of their ease of fabrication. Comb-drive actuators provide high bandwidth and are operated using relatively high voltages [6]. The stroke of these actuators is generally limited by the sideways snap-in of the moving comb at relatively small displacements. We have recently shown that this snap-in phenomenon can be mitigated and delayed by carefully designing the guidance flexure of the comb-drive actuator. Consequently, strokes as high as 245 μm per direction were achieved with 1 mm flexure beam length and 6 μm comb gap in a single direction at approximately 120 V [7]. This high stroke enables comb-drive actuators to be implemented in applications that require large displacement. In this paper, we extend this single-axis electrostatic actuator concept to a large range electrostatic *XY* micro-stage. Sections 2 and 3 present the design and analysis of the proposed *XY* stage. Finite element analysis results are presented in section 4 to simulate the vibration mode shapes of the device. Section 5 summarizes the fabrication process and the experimental results demonstrating bi-directional displacement of 225 μm per axis in the *XY* stage.

2. *XY* stage design

2.1. Electrostatic comb-drive actuators background

Theoretical analysis of electrostatic comb-drive actuators has been extensively discussed in earlier literatures [6, 7, 21]. Here a summary of comb-drive snap-in is presented since it provides the foundation for subsequent sections. A linear in-plane electrostatic comb-drive actuator comprises two electrically isolated conductive combs (fixed and moving) with *N* fingers each, schematically shown in figure 1. The moving comb is guided via a flexure mechanism with relatively low stiffness (K_m) in the motion direction, and relatively high stiffness (K_b) in the bearing direction. When a voltage difference (V) is applied between the two combs, they experience an electrostatic attractive force, which displaces the moving comb by Y along the motion direction:

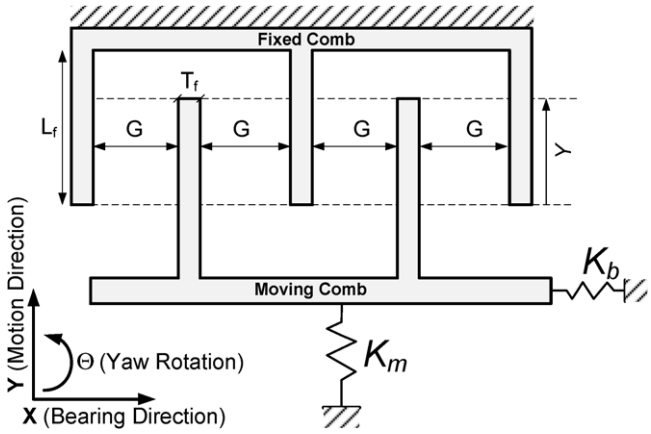

Figure 1. Schematic of an electrostatic comb drive with the springs representing the flexure bearing.

$$K_m \cdot Y = \frac{\varepsilon_o H}{G} N V^2. \quad (1)$$

Here, ε_0 is the dielectric constant of air, G is the comb gap, and H is the out-of-plane thickness. The maximum displacement (stroke) is limited by the snap-in phenomenon, which corresponds to sideways instability of the moving comb [21]. For any Y displacement, the electrostatic force due to the actuation voltage V produces a destabilizing or negative spring effect and the flexure mechanism offers a stabilizing or positive spring effect in the X direction. The former increases while the latter generally decreases with increasing Y displacement. At the Y displacement at which the former stiffness exceeds the latter, the moving comb snaps sideways into the static comb. This condition determines the maximum actuation stroke of the actuator and is mathematically expressed as [22]:

$$\left(\frac{K_b}{K_m}\right) \geqslant \frac{2Y^2}{G^2}(1+S). \quad (2)$$

Table 2. Electrostatic comb-drive based micro *XY* stages.

Reference	*X* displacement (μm) @ (V)	*Y* displacement (μm) @ (V)	Resonant Frequency (Hz)	Foot-print (mm^2)	Beam length (μm)	Design (flexure)
[4]	24 (180)	24 (180)	2090	4 × 4	1375	P. K. (FB)
[26]	19 (110)	23 (60)	–	2 × 2	550, 850	S. K. (FB)
[2]	110 (70)	90 (125)	690	2.5 × 2	645	S. K. (pre-bent DP)
[3]	±18 (6)	±18 (6)	164	–	725	P. K. (triple DP-DP)
[31]	±3 (150)	±3 (150)	10000	–	–	P. K. (B)
[5]	55 (40)	55 (40)	280	3 × 3	795	P. K. (L shape beam)
[32]	10 (70)	10 (70)	–	–	–	P. K. (B)
[30]	±12.5 (30)	±12.5 (30)	–	4 × 4	421.5	P. K. (B)
[33]	±50	±50	739	14 × 14		P. K. (P)
[34]	±10 (23)	±10 (23)	–	1.6 × 1.6	1200	P. K. (DP-DP)
Current Work	228 (94)	228 (94)	400	4 × 4	1000	P. K. (C-DP-DP)

P. K. = parallel kinematic configuration, S. K. = serial kinematic configuration, B = simple beam, FB = folded beam, P = parallelogram flexure, DP = double parallelogram flexure, C-DP-DP = clamped paired double parallelogram flexure.

The right-hand side represents a 'critical K_b/K_m stiffness ratio' needed to avoid snap-in, and clearly has to be large if a large actuation stroke is desired. Here, S is a positive margin of stability to account for the increase in the required K_b/K_m stiffness ratio when an error motion (E_x) is present. E_x includes any motion or misalignment of the moving comb in the X direction with respect to its nominal zero position due to flexure mechanics or fabrication imperfections, in the absence of electrostatic force. Clearly, to delay snap-in and maximize the actuator stroke, the flexure mechanism should provide a high (K_b/K_m) ratio over a large Y displacement range.

2.2. Serial versus parallel kinematics

XY stages can be designed in serial-kinematic or parallel-kinematic configurations [4, 23, 24]. Both these configurations present unique challenges in meeting the large range motion objective. A serial kinematic *XY* stage is simply constructed by serially stacking one single-axis stage on the other. In fact, most macro-scale machines and metrology tools and many micro *XY* stages [25, 26] are built this way. This configuration leads to the actuator of the second axis being mounted on the motion stage of the first axis. This moving actuator and associated moving electrical connection present a challenge in MEMS fabrication and operation. Furthermore, this arrangement can cause the moving inertia load associated with the two axes and corresponding resonant frequencies of the axes to be different [27]. Except for applications that need a fast and slow axis such as scanning probe microscopy [28], such an attribute may not be desirable, in general. A parallel kinematic configuration, on the other hand, does not suffer from these drawbacks because of ground-mounted actuators. One of the most commonly implemented configurations for a comb-drive based micro *XY* stage employs a moving stage connected to the four surrounding identical comb drives via four sets of slender flexure beams [29, 30]. However, parallel-kinematic designs often suffer from cross-axis coupling errors as well as kinematic over-constraint, both of which lead to a restricted motion range. A summary of existing micro *XY* stages actuated by electrostatic comb drives and their respective stroke are presented in table 2. Our proposed design is explained in the next section.

2.3. Proposed design principle for XY micro-stage

The configuration of the proposed *XY* micro-stage is shown in figure 2. There are four rigid stages: ground, motion stage, and two intermediate stages. The motion stage has two translational degrees of freedom with respect to ground. The intermediate stages are necessary to decouple the motion between the two axes and isolate the associated actuators from each other. The rigid stages in figure 2 are inter-connected by means of flexure modules that act as frictionless bearings and constrain relative motion. Each flexure module is a single degree of freedom mechanism that only allows translation in its respective motion direction and high stiffness in all other directions. The first intermediate stage is connected to ground by means of the first guidance flexure, which only allows relative displacement along the X direction and constrains all the other degrees of freedom. This implies that irrespective of the rest of the mechanism, the first intermediate stage will have a primarily X displacement with respect to ground.

The first intermediate stage is connected to the motion stage by means of the first transmission flexure that allows for relative displacement in the Y direction only and constrains all other degrees of freedom. This implies that the X displacement of the first intermediate stage will be largely transmitted to the motion stage, while any Y displacement of the motion stage will not influence the first intermediate stage. Thus, the first intermediate stage becomes an ideal location for integrating the X actuator. The first guidance flexure provides a linear guide/bearing for the X actuator. Furthermore, any X force applied at the first intermediate stage produces minimal Y motion of the motion stage due to the isolation provided by the first transmission flexure. Analogous arguments hold true for the second intermediate stage, the second guidance flexure, and the second transmission flexure, which collectively provide Y displacement at the motion stage.

Ideally, in any deformed configuration of the flexure mechanism, the first intermediate stage always has an X displacement while the second intermediate stage has a Y displacement. The motion stage inherits the X displacement of first intermediate stage and the Y displacement of second intermediate stage, thus acquiring two translational degrees of freedom. Since all the connecting flexure units individually

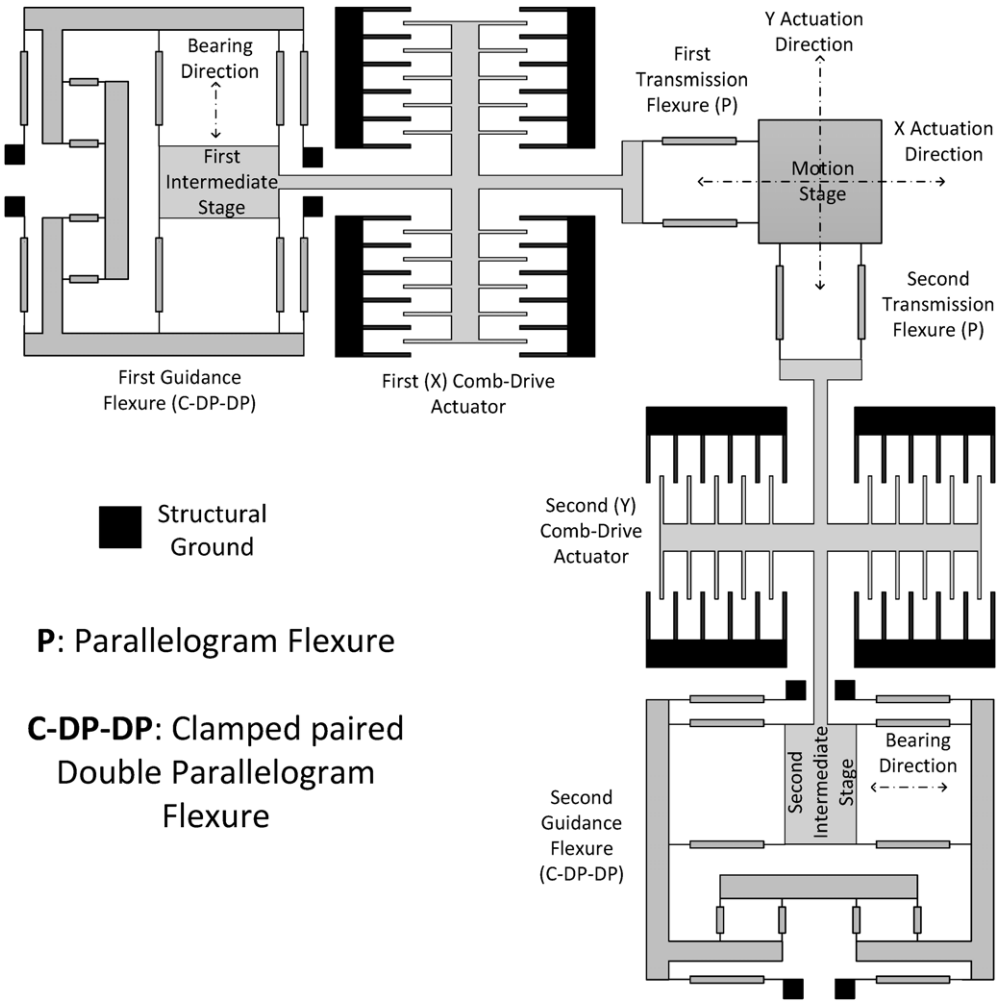

Figure 2. Proposed design of the comb-drive based *XY* micro-stage.

constrain rotation, the rotation of the motion stage is also constrained with respect to ground. This is an idealized scenario, where all guidance and transmission flexures are perfect single degree of freedom constraints. In reality, any flexure module will have finite compliance and range of motion along its degrees of freedom, and finite stiffness along its bearing or constraint directions. As a result, there will be finite error motions in the overall *XY* stage, the extent of which depends on the flexure modules that are chosen.

In the proposed *XY* micro-stage layout, the electrostatic comb-drive actuator for each axis is placed between ground and the respective intermediate stage for that axis and the respective guidance flexure provides guidance between the fixed and moving combs of the actuator. The guidance flexures should offer high bearing direction stiffness (K_b) while maintaining low motion direction stiffness (K_m) over a large range of motion direction displacement, in order to mitigate the onset of sideways snap-in instability induced by the electrostatic actuation forces. These stiffness attributes in the guidance flexure help increase the actuation stroke along each axis in the proposed micro *XY* stage. A flexure module that is suitable for guidance of the intermediate stages is the clamped paired double parallelogram (C-DP-DP) flexure as shown in figures 2 and 3, and introduced in our previous paper [7]. The main function of the transmissions flexures is to transmit the motion from the intermediate stage to the motion stage with minimal motion loss and with the smallest possible mass and footprint. Moreover, the transmission flexure module in the *X* direction should provide minimal stiffness, i.e. resistance to motion, in the *Y* direction, and vice versa. The parallelogram (P) flexure satisfies these needs effectively with a small footprint. To get the best motion performance at the motion stage, one needs to optimize the dimensions of C-DP-DP and P flexures along with the comb-drive actuators. In the next section, these dimensions are chosen based on a closed form analysis [7, 35].

3. Analysis

This section presents a closed form analysis of the key performance characteristics of the proposed *XY* micro-stage, including stroke (Y_{max}), actuation effort (NV^2), first resonant frequency, and actuator error motion (δ). We define the latter as the undesired motion along bearing direction of one actuator due to the motion direction displacement of the other actuator. Note that there are two comb-sets per actuation axis to provide

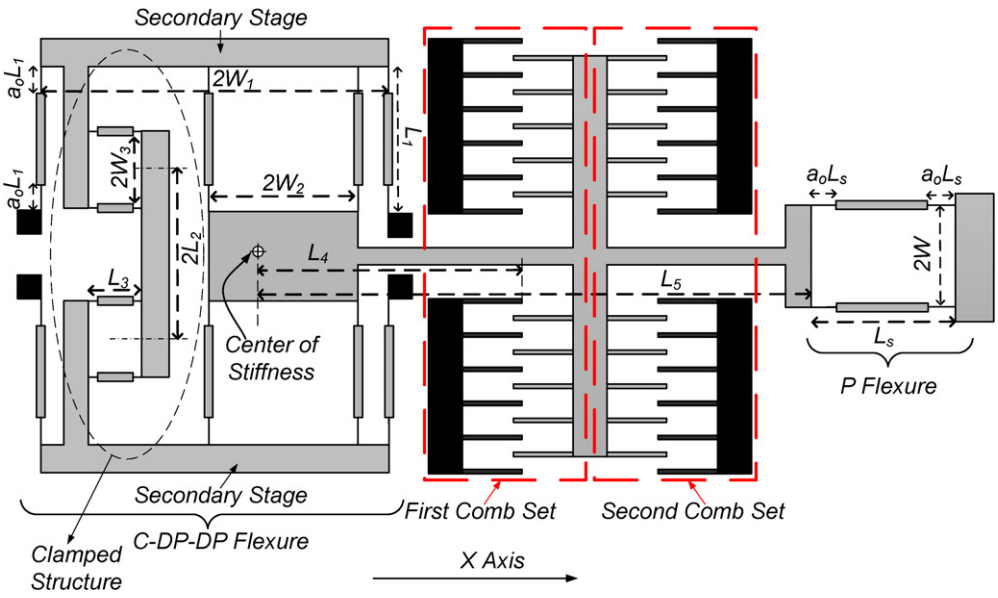

Figure 3. Detailed view of *X* actuator with two comb-sets. (*H*: device depth, T_1: beam thickness.)

bi-directional actuation capability along each axis. The first comb-set in figure 3 provides actuation along the negative *X* axis, while the second comb-set provides actuation along the positive *X* axis.

3.1. Actuation stroke and effort

The analytical relations for the motion and bearing stiffness of the C-DP-DP and P flexures have been separately derived [36]. For the case of optimal clamp dimensions $\left(W_3^2L_1^3\right)/\left(2L_2^2L_3T_1^2\right) > 100$ the motion direction and bearing direction stiffness values for the C-DP-DP and P flexure are equal and are expressed in equation (3). The rotational stiffness of these two flexures is expressed in equation (4):

$$K_m = \frac{2EIk_{11}^{(0)}}{L^3} \qquad K_b = \frac{2EI}{L^3}\frac{k_{33}}{\left(1+k_{33}g_{11}^{(1)}\left(\frac{Y}{2L}\right)^2\right)} \tag{3}$$

$$K_\theta|_{\mathrm{C-DP-DP}} = \frac{2W_1^2W_2^2}{\left(W_1^2+W_2^2\right)}K_b; \qquad K_\theta|_P = W^2K_b. \tag{4}$$

Here, *E* is the Young's modulus of the material and *I* is the second moment of area ($= HT_1^3/12$). All the dimensions that appear in these formulae are defined in figure 3. The non-dimensional terms $k_{11}^{(0)}$,$k_{11}^{(1)}$,$g_{11}^{(1)}$, and k_{33} are all functions of the beam shape (a_o and T_1, shown in figure 3) and are referred to as beam characteristic coefficients [37]. These terms are mathematically expressed as follows:

$$k_{11}^{(0)} = \frac{6}{\left(3-6a_o+4a_o^2\right)a_o}$$

$$k_{11}^{(1)} = \frac{3\left(15-50a_o+60a_o^2-24a_o^3\right)}{5\left(3-6a_o+4a_o^2\right)^2}$$

$$g_{11}^{(1)} = \frac{2a_o^3\left(105-630a_o+1440a_o^2-1480a_o^3+576a_o^4\right)}{175\left(3-6a_o+4a_o^2\right)^3}$$

$$k_{33} = \frac{6}{a_0(T_1/L)^2}. \tag{5}$$

Considering the equivalent mass-spring system of the proposed *XY* stage in any one direction, the motion direction stiffness is calculated as:

$$K_m = K_{m(\mathrm{C-DP-DP})} + K_{m(P)} = \frac{2EI_1}{L_1^3}k_{11}^{(0)} + \frac{2EI_s}{L_s^3}k_{11}^{(0)}$$
$$= \frac{EHT_1^3}{6L_1^3}k_{11}^{(0)}\left(1+\left(\frac{L_1}{L_s}\right)^3\left(\frac{T_s}{T_1}\right)^3\right). \tag{6}$$

This equation is derived for a general case, where the beam length and thickness of the P flexure are different from C-DP-DP flexure and are L_s, and T_s, respectively. As mathematically expressed in equations (1) and (2), K_m should be minimized in order to achieve large stroke $Y_{\max}$, and small actuation effort, NV^2. This, in turn, implies that T_1 should be minimized. In fact, the smallest value of T_1 is usually dictated by the practical limits of the micro-fabrication process. Furthermore, it can also be shown that in order to minimize K_m, T_s should be equal to T_1. Next, the effective bearing direction stiffness at each actuator comb-drive location (K_{bnet}) is given by:

$$K_{\mathrm{bnet}} = \left(\frac{1}{K_b}+\frac{1}{\frac{K_\theta}{L_4^2}}\right)^{-1} \Rightarrow$$
$$K_{\mathrm{bnet}} = K_b\left(\frac{2W_1^2W_2^2}{2W_1^2W_2^2+L_4^2\left(W_1^2+W_2^2\right)}\right), \tag{7}$$

where L_4 is the distance from center of stiffness (CoS) of the C-DP-DP flexure to the tips of the stationary comb fingers, for any given axis, as shown in figure 3. CoS is the particular location in the C-DP-DP mechanism, where an applied bearing direction force results in zero rotation of the intermediate stage. The maximum stroke ($Y_{\max}$) of the micro *XY* stage is calculated by substituting K_{bnet} and K_m in equation (2):

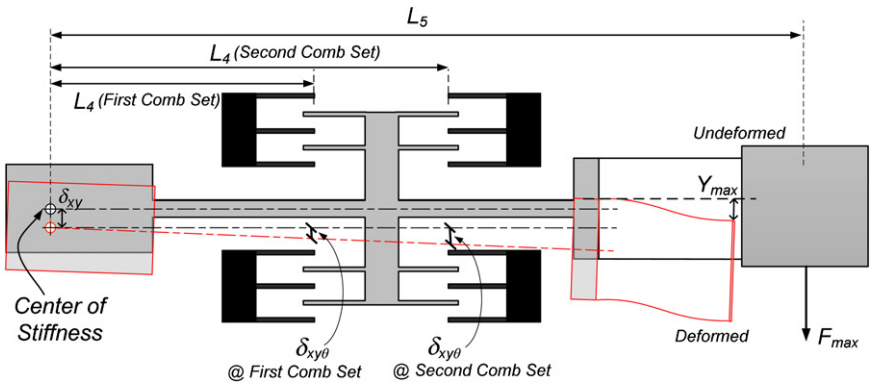

Figure 4. Displacement ($\delta = \delta_{xy} + \delta_{xy\theta}$) of the comb fingers due to $Y_{\max}$ at the motion stage. δ_{xy} is the displacement due to force $F_{\max}$, and $\delta_{xy\theta}$ is the displacement due to moment $M_{\max} = F_{\max}L_5$.

Table 3. Dimensions of the *XY* stages. All the dimensions are in micrometers (μm).

G	T_f	N	L_f	T_1	L_1	L_2	L_3	L_4	L_5	L_s	W_1	W_2	W_3	H_1	a_0
6	4	140	175	3	1000	850	430	1385, 1550	3800	1000	775	250	240	50	0.2

$$Y_{\max} = L_1\sqrt{\frac{2}{k_{33}g_{11}^{(1)}}\left(\sqrt{1+\left(\frac{G}{L_1}\right)^2\frac{(k_{33})^2 g_{11}^{(1)}\Phi}{2k_{11}^{(0)}(1+S)}}-1\right)}$$

where,

$$\Phi = \left(\frac{2W_1^2W_2^2}{2W_1^2W_2^2 + L_4^2\left(W_1^2+W_2^2\right)}\right)\frac{1}{\left(1+\left(\frac{L_1}{L_s}\right)^3\right)}. \quad (8)$$

In the above $Y_{\max}$ relation, the second term in the second square root is typically two orders of magnitude larger than one. For instance, this value is 147 with the dimensions listed in table 3. Therefore, the $Y_{\max}$ relation can be further simplified as follows by assuming $L_1 = L_s$:

$$Y_{\max} = L_1\sqrt{\frac{2}{k_{33}g_{11}^{(1)}}\left(\left(\frac{G}{L_1}\right)(k_{33})\sqrt{\frac{g_{11}^{(1)}\Phi}{2k_{11}^{(0)}(1+S)}}-1\right)}. \quad (9)$$

The actuation effort (NV^2) needed to achieve this stroke is found by substituting this displacement value in equation (10):

$$\frac{NV^2}{G} = \frac{k_{11}^{(0)}}{6}\left(\frac{E}{\epsilon_0}\right)\left(\frac{T_1}{L_1}\right)^3\left(1+\left(\frac{L_1}{L_s}\right)^3\right)Y_{\max}. \quad (10)$$

3.2. Actuator error motion in comb-drive sets due to the cross-axis displacement of the motion stage

The transmission flexures connect the intermediate stages to the motion stage. Referring to figure 3, ideally the *X* axis transmission flexure should provide a single translational DoF along the *Y* direction, i.e. zero compliance in this direction. This would ensure that a *Y* direction displacement of the motion stage does not produce any *Y* direction (i.e. bearing direction) error motions at the first intermediate stage and first guidance flexure. However, in practice, since the P transmission flexure has a finite compliance in the *Y* direction, the *Y* displacement of the motion stage does produce a small bearing direction displacement at the intermediate stage of the *X* actuator. We refer to this undesired motion as the actuator error motion, which reflects a lack of perfect actuator isolation [23, 38]. This error motion in the comb-drive sets introduces a destabilizing force, thus increasing the critical stiffness ratio in equation (2), and consequently reducing the $Y_{\max}$. In this section, a formulation for calculating this error motion at the comb-derive sets, and its influence on the early snap-in of the comb sets is presented. Any *Y* displacement of the motion stage exerts a force at the first intermediate stage at the distance of L_5 from the CoS of the *X* direction C-DP-DP flexure, shown in figure 4. The maximum value of this force ($F_{\max}$), which occurs when $Y = Y_{\max}$, is:

$$F_{\max} = \left(\frac{2EI_1}{L_s^3}k_{11}^{(0)}\right)Y_{\max}. \quad (11)$$

This force and the resultant moment around the CoS tend to displace the comb fingers in the bearing direction from their nominal centered position. This displacement, which is greater for the second comb-set because of its geometric location, is given by:

$$\delta = \delta_{xy} + \delta_{xy\theta} = \left(\frac{F_{\max}}{K_b} + \frac{F_{\max}L_4L_5}{K_\theta}\right) \Rightarrow$$
$$\delta = k_{11}^{(0)}Y_{\max}\left(\frac{1}{k_{33}} + g_{11}^{(1)}\left(\frac{Y_{\max}}{2L_1}\right)^2\right)\left(\frac{L_1}{L_s}\right)^3$$
$$\times\left(1+\frac{L_4L_5\left(W_1^2+W_2^2\right)}{2W_1^2W_2^2}\right). \quad (12)$$

This displacement appears as error motion ($E_x = \delta$) in equation (2), and therefore reduces the $Y_{\max}$. This implies that, to accommodate this error motion, one has to employ a finite stability margin (S), which is mathematically captured previously [7, 22]. For instance, with the current dimensions of the *XY* stage listed in table 3, the following values are obtained. Assuming $\delta = 0$ and therefore $S = 0$, one can show that $Y_{\max} = 138\ \mu$m. However, for these actual *XY* dimensions,

one can calculate $\delta = 0.18\ \mu$m, which corresponds to $S = 0.22$. With this new value of required stability margin, the actuation stroke reduces to $Y_{\max} = 130\ \mu$m:

$$S = \left(1 + \frac{3X_c^2}{G^2}\right) \Big/ \left(1 - \frac{X_c^2}{G^2}\right)^2 - 1$$

where

$$\delta = E_x = \frac{4X_c^3}{G^2 + 3X_c^2}. \tag{13}$$

3.3. Resonant frequency

The resonant frequency of the stage is calculated by equation (14). This equation is derived using the Rayleigh's energy method, i.e. by equating the total maximum kinetic energy during the vibration cycle to the maximum potential energy [39]:

$$f_{\text{res}} = \frac{1}{2\pi}\sqrt{\frac{K_m}{M}} = \frac{1}{2\pi}\sqrt{\frac{\frac{Ek_{11}^{(0)}}{6}\left(1 + \left(\frac{L_1}{L_s}\right)^3\right)\left(\frac{T_1}{L_1}\right)^3}{\rho\left(A_p + \frac{1}{4}A_s\right)}}. \tag{14}$$

In this equation A_p and A_s represent the area of parts moving at the velocity of the motion stage and half that velocity, respectively.

3.4. Design summary

This section summarizes a step-by-step procedure to determine the various dimensions of the *XY* stage, including L_1, L_s, T_1, a_0, W_1, W_2, W, L_2, L_3, W_3, and G. The goal here is to maximize the actuation stroke while minimizing the device footprint and actuation voltage. A similar procedure to design large-stroke single-axis comb-drive actuators and associated guidance flexures was presented in detail in [7]; here, we extend that procedure to the proposed *XY* micro-stage. The guidance and transmission flexures should offer high bearing direction stiffness (K_b) while maintaining low motion direction stiffness (K_m), over a large range of motion direction displacement. We start the design process with an assumed nominal value of $L_1 = L_s = 1$ mm for the length of flexure beams. The flexure beam thickness (T_1) is chosen to be a small value to lower the actuation effort and reduce the bending stress in the flexure beams. This value is dictated by the practical limits of the micro-fabrication process, $T_1 = 3\ \mu$m. The beam shape $a_0 = 0.2$ is chosen to double the K_b/K_m stiffness ratio for the same flexure beam thickness T_1. Comb-gap $G = 6\ \mu$m is chosen to maximize stroke ($>100\ \mu$m per direction of each axis) while minimizing the actuation effort NV^2. Finally, W_1, W_2, L_2, L_3, W_3 and W are chosen such that rotational stiffness K_θ given by equation (4) and the clamp effectiveness parameter $\left(\left(W_3^2 L_1^3\right)/\left(2L_2^2 L_3 T_1^2\right)\right)$ are adequately high to not degrade the desired designed stroke [7]. All the dimensions of the stage are listed in table 3.

4. Mode shape analysis

In order to validate the theoretical analysis results of the previous sections and further evaluate the dynamic performance of the system under consideration, finite elements analysis (FEA) was conducted using the commercial software (COMSOL). Here, we specifically present the outcome of the modal analysis that was performed. The following material properties were used: density $\rho = 2330$ kg m^{-3}, Young's modulus $E = 164$ GPa, and Poisson's ratio $\upsilon = 0.28$. The first six mode shapes and their corresponding natural frequencies are shown in figure 5.

The first and second mode shapes correspond to the translational vibration of the first intermediate stage, the second intermediate stage, and the motion stage, and appear at around 418 Hz. The deformations of C-DP-DP and P flexures seen here validate the conditions used in estimating the first resonant frequency in equation (14). Compared to the analytical result obtained in the previous section (414 Hz), the FEA result is approximately 1% lower.

Due to the symmetry along the diagonal direction of the motion stage, the first and second modes, the third and fourth modes, the sixth and seventh modes (latter not shown), etc, appear as pairs with their natural frequencies close to each other. The third and fourth modes primarily involve the vibration of the secondary stages and the external clamp in both the C-DP-DP guidance flexures, while the two intermediate stages and the motion stage experience relatively little displacement. The fifth mode is an out-of-plane mode shape that captures the vertical vibration of the intermediate stages and motion stage. This out-of-plane mode appears before many in-plane modes, due to the relatively smaller out-of-plane stiffness of the flexure modules compared to their in-plane stiffness. Finally, the sixth and seventh modes, which are not shown, capture the in-plane vibration of the external clamp by itself within the C-DP-DP flexure modules.

5. Experimental results and discussion

5.1. Fabrication

The *XY* micro-stages were fabricated using silicon on insulator (SOI) wafers with a device layer of 50 μm, a buried oxide layer of 2 μm, and a silicon handle layer of 350 μm. The device layer of the SOI wafers is heavily boron doped (P type) with resistivity less than 0.01 Ω.cm. The silicon device layer was first patterned and etched by deep reactive ion etching (DRIE), and then the silicon handle layer was patterned and etched by DRIE. Finally, buried oxide was removed by hydrofluoric (HF-49%) acid. After the last etching process, a critical point dryer was used to dry the samples to avoid stiction [40]. In this drying method, liquid CO_2 is transferred to vapor via the supercritical phase (@ $T_c = 38^\circ$, $P_c = 80$ atm) to avoid capillary forces that arise from the surface tension at the liquid–vapor interface. Scanning electron microscope (SEM) images of a representative fabricated device is shown in figure 6.

5.2. Voltage–stroke curves

The fabricated comb-drive actuators were excited by applying dc voltages (Keithley 4200SCS) via connecting wires (Alessi probe station) to the fixed and moving combs. The voltage was swept in a ramp profile with 1 V increments from zero to a

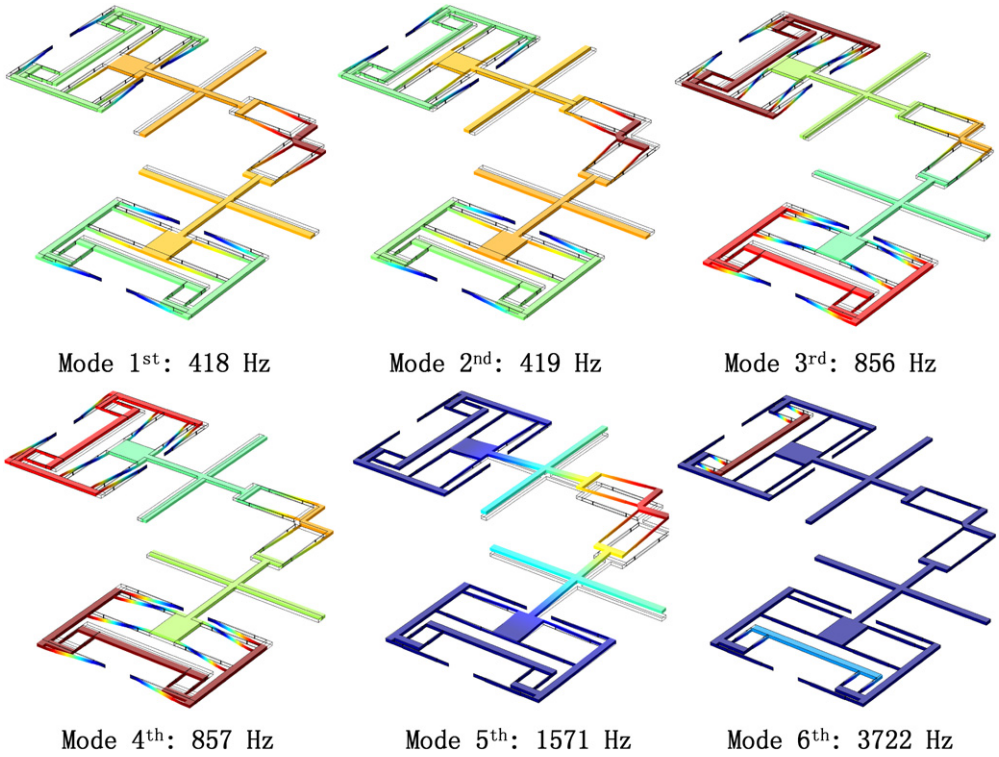

Figure 5. The first six mode shapes of the micro-stage (red and brownish colors represent largest displacement as opposed to blue color which represents least displacement).

Table 4. Comb-drive *XY* stage resonant frequency and static displacement.

		First resonant frequency (Hz)			Predicted/designed stroke (μm)		Measured	Voltage at
	L_4 (μm)	Theoretical	FEA	Measured	$S = 0$	$S = 1$	stroke (μm)	stroke (V)
First comb set	1385	414	418	400	139	115	124	94
Second comb set	1825				120	99	104	86

maximum of the actuator snap-in voltage. The displacement response of the actuators was observed with a microscope and captured by a CCD camera. Subsequently, the displacement of the actuators was quantitatively measured using image processing software. The motion direction displacement measurements were repeatable within 1 μm.

Figure 7 demonstrates the displacement versus voltage curves for the first and second comb sets of the *X* axis actuator in the *XY* micro-stage. The measured stroke for the first and second comb set is 124 μm and 104 μm, respectively (table 4). The measured strokes of the comb sets are different because the values of L_4 for the two comb sets are different. L_4 is the distance from the tip of comb finger to the CoS of the guidance flexure, as shown in figure 4, and is 1385 μm and 1550 μm for the first and second comb sets, respectively. A larger L_4 will reduce the effective bearing direction stiffness, as seen in equation (7), and consequently results in a smaller stroke. With a stability margin of $S = 1$, the theoretical stroke calculated from equation (8) for these two comb sets is 115 μm and 99 μm, respectively. The difference between the experimentally measured stroke and the theoretically calculated stroke corresponds to errors of 7% and 4%, indicating that $S = 1$ is a reasonable stability margin to be implemented in the theoretical prediction of actuation stroke.

Figure 7 presents a plot of the theoretical *Y* displacement versus actuation voltage. The theoretically (equation (10)) predicted and experimental results for these two cases agree within 22% and 17%, in the order that they are presented above. These discrepancies are within the expected range of deviation given the multiple sources of variability and uncertainty in dimensions and material properties in micro-fabricated devices.

To demonstrate that the fabricated *XY* micro-stage is capable of simultaneous *X* and *Y* motion, a 180 μm by 180 μm square, is scanned using the fabricated device. The cross-talk error of the motion stage (undesired displacement along one axis of motion stage generated by the actuation of the other axis) is measured and compared with FEA simulation results as demonstrated in figure 8. For this experiment, the *X* actuator was excited by dc voltage in a ramp profile from 0 to 80 V, and the displacement of motion stage in the *Y* direction was observed through the microscope. Cross-talk error of motion stage in the *Y* direction was 3.6 μm at 80 V. At 80 V the displacement of the motion stage at the *X* direction is around 90 μm. FEA predicts cross-talk error of 2 μm in the *Y* direction for 90 μm displacement in the *X* direction.

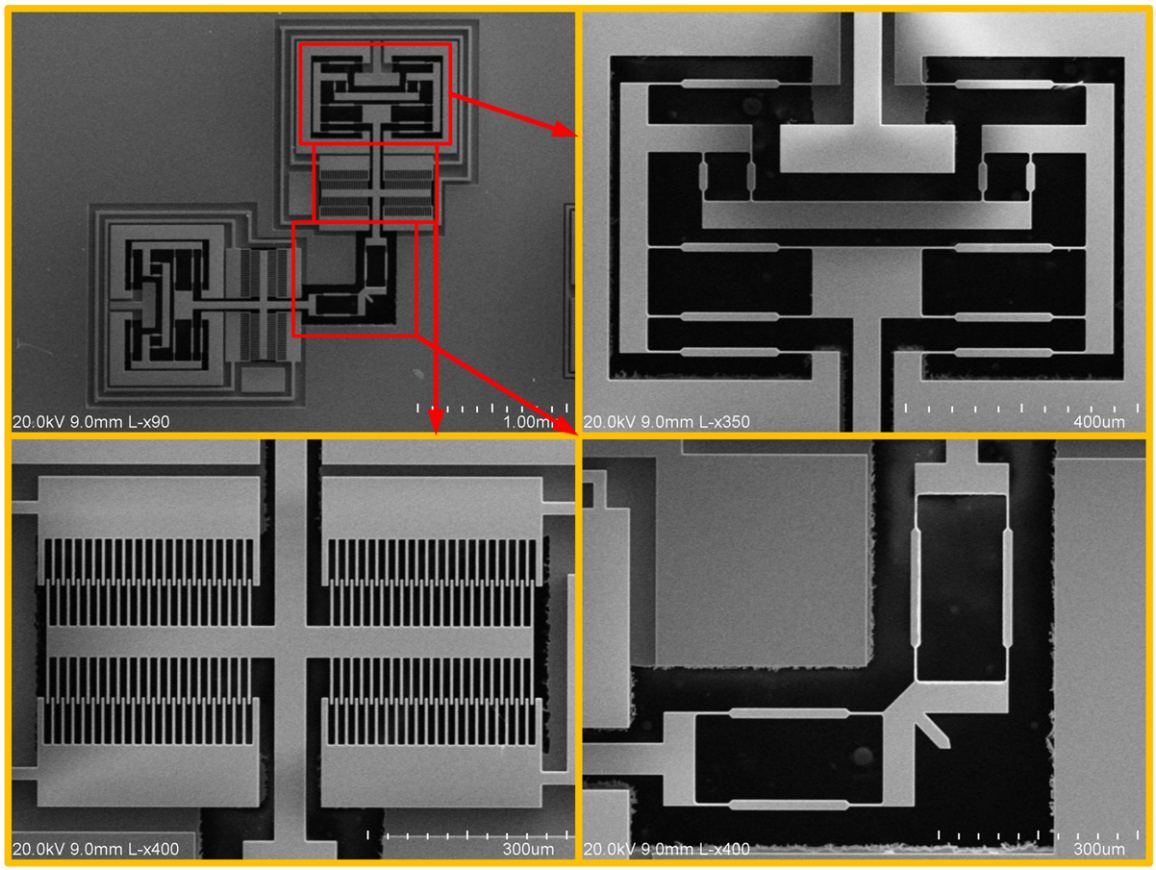

Figure 6. SEM image of a micro-fabricated *XY* stage.

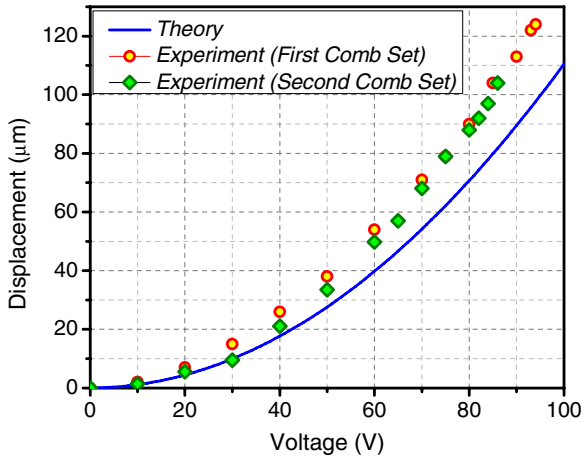

Figure 7. *Y* displacement versus voltage for the first and second comb set of the micro-stage.

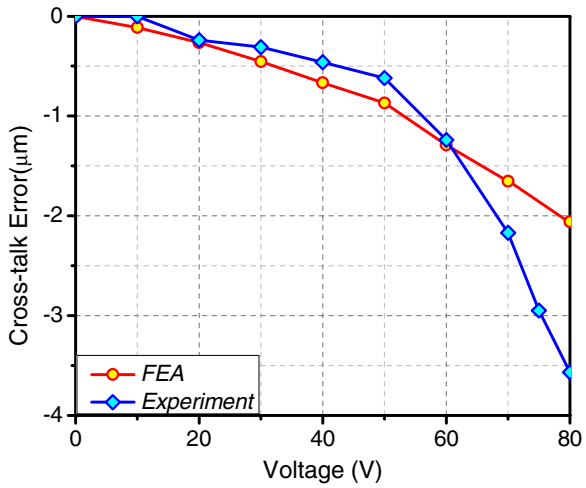

Figure 8. Experimental and FEA analysis of cross-talk error of the motion stage.

The motion range of the current device is compared to that of previously reported devices in the literature in figure 9. It has been previously shown that the maximum actuation stroke of single-axis comb-drive actuators based on flexure mechanisms that employ parallel beams (e.g. P, DP, DP-DP, C-DP-DP, etc) can be expressed as follows [7]:

$$Y_{\max} \propto \lambda \left(N V_{\max}^2\right)^{1/3} \quad (L_1)^{4/3}. \tag{15}$$

The first term on the right-hand side of this equation (λ) depends on the stiffness and error motion characteristics of the flexure mechanism used and incorporates the various flexure mechanism dimensions. The second term represents actuation effort and device footprint (due to N), and should therefore be minimized. The third term, although not the actual device footprint, is representative of the device footprint and therefore should also be minimized. Although the above expression is derived for single-axis electrostatic comb-drive actuators, we use it to compare *XY* electrostatic comb-drive actuators as well because the underlying physical relations remain the same. The

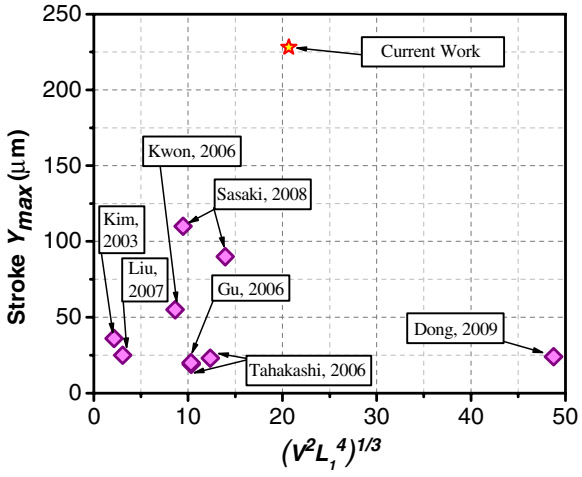

Figure 9. Comparison of the results of the tested micro-stage in this paper with previously reported comb-drive *XY* stages (*V* and L_1 are in volts and mm, respectively).

horizontal axis in figure 9 is a representation of the actuation effort and the device footprint. The value of *N* is not included in this figure since it was not reported in many of the previously published papers. This figure shows the large motion range capability of the proposed *XY* micro-stage design.

5.3. Resonant frequency

The dynamic behavior (resonant frequency) of the stage is tested experimentally by implementing the 'blur envelope' technique [39]. In this technique, the resonant frequencies are determined by changing the frequency of an input drive signal of the form of ($V_{in} = V_p + V_d\text{Sin}(\omega t)$) until a blur envelope of the vibrating structure is observed. Since the excitation force depends on $(V_{\text{in}})^2$, the terms $V_pV_d\text{Sin}(\omega t)$ and $(V_d)^2\text{Cos}(2\omega t)$ appear in the steady state response. To avoid the appearance of these two terms in the steady state response one can choose $V_p \gg V_d$ or $V_p \ll V_d$ based on the experimental conditions. It is worth mentioning that in the case of $V_p \ll V_d$, the frequency of the drive signal must be set to half that of the resonant frequency of the structure.

In our experiments, a sinusoidal drive signal in the form of ($V = 3 + 50\text{Sin}(\omega t)$) was generated by a signal generator (HP/Agilent 33220A) and amplified by a voltage amplifier (Avtek-110B). First, a frequency sweep was conducted to locate the device's resonant frequency. Then, careful measurements were taken around that frequency to locate the exact value of the device's resonant frequency. The measured resonant frequency was 400 Hz, which is approximately 4% smaller than the theoretically and FEA predicted values, as shown in table 4. The source of this discrepancy is most likely the dimensional variations in the micro-fabricated device.

6. Conclusion

XY micro-stages with a bi-directional displacement range greater than 225 μm per axis and a bandwidth of 400 Hz are reported in this paper. Possible applications include probe-based data-storage systems, scanning probe microscopy, and optical sensing and communication systems. The large range reported in this paper has been achieved by implementing the C-DP-DP flexure as the guidance flexure and the P flexure as the transmission flexure in the *X* and *Y* directions. The fabricated micro-stage is capable of simultaneous *X* and *Y* motion, a 180 μm by 180 μm square, is scanned using the fabricated device. The cross-talk error of the motion stage is measured and it is around 3% of the motion displacement at the highest level. The cross-talk error at 90 μm displacement (@80 V) of the motion stage is around 3 μm.

Acknowledgments

This research was supported, in part, by a National Science Foundation grant (CMMI # 0846738). The experimental portion of this work was performed at the Lurie Nanofabrication Facility, a member of the National Nanotechnology Infrastructure Network, which is also supported in part by the National Science Foundation.

References

[1] Eleftheriou E *et al* 2003 Millipede—a MEMS-based scanning-probe data-storage system *IEEE Trans. Magn.* **39** 938–45

[2] Sasaki M, Bono F and Hane K 2008 Large-displacement micro-XY-stage with paired moving plates *Japan. J. Appl. Phys.* **47** 3226–31

[3] Kim C H, Jeong H M, Jeon J U and Kim Y K 2003 Silicon micro XY-stage with a large area shuttle and no-etching holes for SPM-based data storage *J. Microelectromech. Syst.* **12** 470–8

[4] Dong J and Ferreira P M 2009 Electrostatically actuated cantilever with SOI-MEMS parallel kinematic XY stage *J. Microelectromech. Syst.* **18** 641–51

[5] Kwon H N, Lee J-H, Takahashi K and Toshiyoshi H 2006 MicroXY stages with spider-leg actuators for two-dimensional optical scanning *Sensors Actuators* A **130** 468–77

[6] Grade J D, Jerman H and Kenny T W 2003 Design of large deflection electrostatic actuators *J. Microelectromech. Syst.* **12** 335–43

[7] Olfatnia M, Sood S, Gorman J J and Awtar S 2013 Large stroke electrostatic comb drive actuators enabled by a novel flexure mechanism *J. Microelectromech. Syst.* **22** 483–94

[8] Brouwer D M, Otten A, Engelen J B C, Krijnen B and Soemers H M J R 2010 Long-range elastic guidance mechanisms for electrostatic comb-drive actuators *Proc. EUSPEN Int. Conf. (Delft)* pp 47–50

[9] Hubbard N B, Culpepper M L and Howell L L 2006 Actuators for micropositioners and nanopositioners *Appl. Mech. Rev.* **59** 324–34

[10] Chen S C and Culpepper M L 2006 Design of contoured microscale thermomechanical actuators *J. Microelectromech. Syst.* **15** 1226–34

[11] Long Q, Jae-Sung P and Gianchandani Y B 2001 Bent-beam electrothermal actuators: part I. Single beam and cascaded devices *J. Microelectromech. Syst.* **10** 247–54

[12] Syms R R A 2002 Long-travel electrothermally driven resonant cantilever microactuators *J. Micromech. Microeng.* **12** 211–8

[13] Hubbard N B and Howell L L 2005 Design and characterization of a dual-stage, thermally actuated nanopositioner *J. Micromech. Microeng.* **15** 1482–93

[14] Domke J F, Rhee C H, Liu Z, Wang T D and Oldham K R 2011 Amplifying transmission and compact suspension for a low-profile, large-displacement piezoelectric actuator *J. Micromech. Microeng.* **21** 067004
[15] Physik Instrumente GmbH Catalogue 2009 Piezo nano positioning
[16] Kota S, Hetrick J, Li Z and Saggere L 1999 Tailoring unconventional actuators using compliant transmissions: design methods and applications *IEEE/ASME Trans. Mechatronics* **4** 396–408
[17] Soeno Y, Ichikawa S, Tsuna T, Sato Y and Sato I 1999 Piezoelectric piggy-back microactuator for hard disk drive *IEEE Trans. Magn.* **35** 983–7
[18] Lantz M A, Rothuizen H E, Drechsler U, Haeberle W and Despont M 2007 A vibration resistant nanopositioner for mobile parallel-probe storage applications *J. Microelectromech. Syst.* **16** 130–9
[19] Kota S, Joo J, Li Z, Rodgers S M and Sniegowski J 2001 Design of compliant mechanisms: applications to MEMS *Analog Integr. Circuits Signal Process.* **29** 7–15
[20] Chu L L, Hetrick J A and Gianchandani Y B 2002 High amplification compliant microtransmissions for rectilinear electrothermal actuators *Sensors Actuators* A **97–8** 776–83
[21] Legtenberg R, Groeneveld A W and Elwenspoek M 1996 Comb-drive actuators for large displacements *J. Micromech. Microeng.* **6** 320–9
[22] Awtar S and Trutna T 2010 An enhanced stability model for electrostatic comb-drive actuator design *Proc. ASME IDETC/EIX (Montreal, Canada)* pp 597–605
[23] Awtar S 2004 Synthesis and analysis of parallel kinematic XY flexure mechanisms *PhD Thesis* Massachusetts Institute of Technology, Cambridge, MA
[24] Dong J Y, Mukhopadhyay D and Ferreira P M 2007 Design, fabrication and testing of a silicon-on-insulator (SOI) MEMS parallel kinematics XY stage *J. Micromech. Microeng.* **17** 1154–61
[25] Takahashi K, Kwon H N, Saruta K, Mita M, Fujita H and Toshiyoshi H 2005 A two-dimensional f-theta micro optical lens scanner with electrostatic comb-drive XY-stage *IECIE Electron. Express* **2** 542–7
[26] Takahashi K, Mita M, Fujita H and Toshiyoshi H 2006 A high fillfactor comb-driven XY -stage with topological layer switch architecture *IECIE Electron. Express* **3** 197–202
[27] Kenton B J and Leang K K 2012 Design and control of a three-axis serial-kinematic high-bandwidth nanopositioner *IEEE/ASME Trans. Mechatronics* **17** 356–69
[28] Ando T 2012 High-speed atomic force microscopy coming of age *Nanotechnology* **23** 062001
[29] Kim C H and Kim Y K 2002 Micro XY-stage using silicon on a glass substrate *J. Micromech. Microeng.* **12** 103–7
[30] Liu X, Kim K and Sun Y 2007 A MEMS stage for 3-axis nanopositioning *J. Micromech. Microeng.* **17** 1796–802
[31] Indermuhle P F, Jaecklin V P, Brugger J, Linder C, Derooij N F and Binggeli M 1995 AFM imaging with an XY-micropositioner with integrated tip *Sensors Actuators* A **47** 562–5
[32] Hedsten K *et al* 2008 MEMS-based VCSEL beam steering using replicated polymer diffractive lens *Sensors Actuators* A **142** 336–45
[33] Carley L R, Bain J A, Fedder G K, Greve D W, Guillou D F, Lu M S C, Mukherjee T, Santhanam S, Abelmann L and Min S 2000 Single-chip computers with microelectromechanical systems-based magnetic memory (invited) *J. Appl. Phys.* **87** 6680–5
[34] Gu L, Li X X, Bao H F, Liu B, Wang Y L, Liu M, Yang Z X and Cheng B L 2006 Single-wafer-processed nano-positioning XY-stages with trench-sidewall micromachining technology *J. Micromech. Microeng.* **16** 1349–57
[35] Awtar S, Slocum A H and Sevincer E 2007 Characteristics of beam-based flexure modules *J. Mech. Des.* **129** 625–39
[36] Sood S 2013 Analysis of single axis flexure bearing approaching ideal bearing characteristics *Masters Thesis* University of Michigan, Ann Arbor, MI
[37] Awtar S and Sen S 2010 A generalized constraint model for two-dimensional beam flexures: non-linear load-displacement formulation *ASME J. Mech. Des.* **132** 081008
[38] Awtar S and Slocum A H 2007 Constraint-based design of parallel kinematic XY flexure mechanisms *ASME J. Mech. Des.* **129** 816–30
[39] Tang W C 1990 *Electrostatic Comb Drive for Resonant Sensor and Actuator Applications* (Berkeley, CA: University of California)
[40] Tas N, Sonnenberg T, Jansen H, Legtenberg R and Elwenspoek M 1996 Stiction in surface micromachining *J. Micromech. Microeng.* **6** 385–97